

UC Santa Barbara

UC Santa Barbara Previously Published Works

Title

Earthquake collapse mechanisms and periodic, migrating seismicity during the 2018 summit collapse at Kīlauea caldera

Permalink

<https://escholarship.org/uc/item/8xf0n925>

Authors

Alvizuri, Celso R
Matoza, Robin S
Okubo, Paul G

Publication Date

2021-05-01

DOI

10.1016/j.epsl.2021.116819

Peer reviewed

Earthquake collapse mechanisms and periodic, migrating seismicity during the 2018 summit collapse at Kīlauea caldera

Celso R. Alvizuri^a, Robin S. Matoza^b, Paul G. Okubo^c

^a*Institute of Earth Sciences, University of Lausanne*

^b*Department of Earth Science and Earth Research Institute, University of California, Santa Barbara*

^c*Department of Earth Sciences, University of Hawai'i at Manoa, Honolulu, Hawai'i*

Abstract

The 2018 Lower East Rift Zone eruption of Kīlauea volcano was accompanied by a remarkable and periodic succession of collapses in the summit region. Between May-August the eruption and collapse sequence included 54 earthquakes ($M \sim 5$; $M5s$) observed worldwide, and over 45,000 intervening earthquakes ($M \geq 0$). We estimated seismic full moment tensors for the $M5s$ and analyzed the spatiotemporal evolution of the intervening seismicity. The hypocenters were concentrated between 0-3 km depths and reveal arcuate bands that migrated outward by ~ 300 m (map view) and downward by ~ 200 m. The temporal evolution reveals almost daily successions of escalating earthquake swarms, followed by an $M5$, followed by a quiescent period. The moment tensors reveal consistent collapse mechanisms with vertical P-axis orientations. Poisson's ratios estimated from the moment tensors were variable at first ($\nu = 0.1 - 0.3$) and from June 26 onward converged to $\nu \sim 0.28$, similar to loading cycles observed in lab experiments. The shallower collapses approximately follow the expanding contour of the crater, while deeper collapses aggregate first to the north of the previous crater and later to the east and south. We interpret that the magma storage complex beneath the summit region comprises a distributed plexus of cracks that progressively evacuated and underwent collapse as magma drained from the summit region to feed the eruption.

Keywords: Seismic moment tensors, non-double-couple, isotropic, seismicity, caldera collapse, Kīlauea volcano.

1. Introduction

2 On 2018 Kīlauea volcano experienced its largest flank eruption in 200 years
3 and a dramatic collapse of its caldera. The eruption sequence included the
4 largest earthquake on the island in 43 years (magnitude $M6.9$; 2018-05-04), 56
5 other large earthquakes ($M \sim 5$) observed worldwide, and over 70,000 earthquakes

6 ($M \geq 0$) across the island. In total 54 of the $M \sim 5$ events ($M5s$) occurred in the
7 Kīlauea summit region and were concentrated between 0–3 km depths.

8 According to Neal et al. (2019), the 2018 flank eruption and caldera collapse
9 at Kīlauea are characterized by inflationary ground deformation starting mid-
10 March, rising lava lake levels at Pu‘u ‘Ō‘ō and Halema‘uma‘u craters through
11 April, propagating seismicity and lava fountaining towards the Lower East Rift
12 Zone (LERZ). On May 1 the Kīlauea summit region began to deflate and lava
13 lake levels in Halema‘uma‘u began to drop; on May 4 the $M6.9$ earthquake
14 occurred at about 6 km beneath Kīlauea’s south flank. Soon after the $M6.9$
15 earthquake, deflation of Kīlauea’s summit accelerated, and by May 10 the lava
16 lake level had dropped by more than 300 m. Toward the end of May, the summit
17 began to subside in episodic, almost daily patterns, with the crater floor drop-
18 ping by several meters during each episode. These patterns are characterized
19 by escalating earthquake swarms of up to 700 events per day, each followed by
20 an $M5$ and a short period of nominal seismicity levels. The last collapse event
21 occurred on August 2, at about the same time as lava effusion stopped at the
22 LERZ.

23 The 2018 activity at Kīlauea prompted major field sampling and enhanced
24 monitoring by the USGS Hawaiian Volcano Observatory and collaborators which,
25 along with continuously operated networks, offer unprecedented capabilities to
26 observe and interpret sustained eruption and caldera collapse in Hawai‘i. Since
27 1900 only six other caldera collapses have been documented in detail (Gud-
28 mundsson et al., 2016), and seismological studies of caldera collapses include:
29 Piton de la Fournaise, Réunion Island (2007) (Michon et al., 2007), Miyakejima,
30 Japan (2000) (Geshi et al., 2002; Minson et al., 2007; Shuler et al., 2013b), Bár-
31 darbunga, Iceland (2014-2015) (Gudmundsson et al., 2016), and Fernandina,
32 Galápagos Islands (1968) (Simkin & Howard, 1970).

33 In this study, we analyze the collapse events in the Kīlauea summit region; we
34 estimate seismic source mechanisms for the 54 $M5s$ by computing their seismic
35 full moment tensors using waveform data, and analyze spatiotemporal varia-
36 tions in the intervening seismicity using a comprehensive catalog of recently
37 relocated hypocenters for the region. Our results reveal remarkably consistent
38 and episodic collapse mechanisms, with episodic and migrating seismicity.

39 2. Data and Methods

40 We estimated seismic moment tensors for the $M5s$ using waveforms from all
41 possible broadband seismic stations within a 2,000 km radius, available from
42 IRIS-DMC, and hypocenters from a comprehensive catalog of relocated seismic-
43 ity (Matoza et al., 2021). The waveforms were downloaded and processed using
44 ObsPy, a python-based package for seismology (e.g., Krischer et al., 2015).

45 The processing steps for each event were: (1) obtain three-component wave-
46 forms and metadata from IRIS-DMC; (2) remove instrument response using an
47 4-pole Butterworth filter with corner frequencies 0.005, 0.006, 10.0, and 15.0
48 Hz (flat bandpass 0.006–10.0 Hz); (3) using the source-station azimuth and the
49 sensor orientation angle, rotate horizontal components to radial and transverse

50 directions. Additional processing steps, such as cutting time windows and addi-
51 tional bandpass filtering were applied during the moment tensor inversions. In
52 our analysis, the waveforms at near stations (up to ~ 15 km distance) show larger
53 amplitude oscillations that may be related to near field effects, while farther sta-
54 tions (>100 km) show waveforms with lower signal-to-noise ratio. Therefore,
55 for our moment tensor estimates we used data from stations within 15–100 km
56 distances (Figure 1).

57 We estimate full seismic moment tensors and their uncertainties for each
58 event using the methodology described in Alvizuri et al. (2018). The method
59 involves performing an efficient search over the full parameter space of moment
60 tensors (lune longitude, lune latitude, strike, dip, and rake) including magni-
61 tude, and uses a geometric parameterization for moment tensors and their un-
62 certainty quantification (for details and other applications, see e.g. Alvizuri &
63 Tape, 2016; Silwal & Tape, 2016; Alvizuri et al., 2018). For each moment tensor
64 in the parameter space, synthetic seismograms are computed using a frequency-
65 wavenumber approach (Zhu & Rivera, 2002) with a 1D (layered) Earth model,
66 then the seismograms are compared with observed waveforms via a misfit func-
67 tion. The synthetic seismograms for this study were computed using a 1D
68 layered model for the region obtained from CRUST1.0 (Laske et al., 2013).

69 The moment tensor methodology has proven useful for earthquake source
70 characterization for a range of settings in the Earth, including Uturuncu volcano
71 in southwest Bolivia (Alvizuri & Tape, 2016); tectonic events at a subduction
72 zone in southcentral Alaska (Alvizuri et al., 2018); events possibly related to
73 metamorphism in the Himalaya lower crust (Alvizuri & Hetényi, 2019); and
74 nuclear tests and cavity collapses in western USA and in North Korea (Alvizuri
75 et al., 2018; Alvizuri & Tape, 2018).

76 We complemented our moment tensor results by analyzing the temporal and
77 spatial distribution of hypocenters at Kīlauea volcano for 2018. The hypocen-
78 ters are from a recent comprehensive study which relocated seismicity from 32
79 years (1986-2018) for the Island of Hawai’i (Matoza et al., 2021). Their relo-
80 cations were done with the GrowClust algorithm (Trugman & Shearer, 2017)
81 which combines waveform cross-correlation, hierarchical cluster analysis and re-
82 lative relocations; for details, see Matoza et al. (2013, 2021). We focused on the
83 seismicity near Halema’uma’u pit crater in the Kīlauea summit region between
84 longitudes $[-155.30, -155.24]$, latitudes $[19.38, 19.44]$, and depths $[0, 3]$ km (Fig-
85 ure 1). In total, 54 M5s occurred between May-August in the summit region.

86 **3. Results**

87 *3.1. Seismicity*

88 The seismicity at Kīlauea shows three main periods during 2018 (Figure 2):
89 (1) January-April, seismic activity at background levels of about 30 events per
90 day; (2) May-August, activity changes suddenly to 300/day and again to sus-
91 tained levels up to 800/day; (3) August 4-December, activity returns to back-
92 ground levels. Figure 3 shows hypocenters on map and cross sections for the
93 three periods above.

94 During the first period (Jan-May) the seismicity was concentrated beneath
95 the summit region and was typical for the region (with approximately the same
96 distribution from 1986-2017). The seismicity occurred from the surface to about
97 3 km below sea level (bsl) and from 7-13 km bsl, and in the upper West and
98 upper East Rift Zones from 1-3 km bsl. The gap between \sim 3-7 km is attributed
99 to the relatively aseismic magma storage reservoir. The next period (May-Aug)
100 shows elevated seismicity in the summit region and along ERZ (depths 3-7 km
101 bsl). In the next period (Aug-Dec) the seismic activity decreased to background
102 levels (though slightly more elevated than 2017 levels), and increased beneath
103 Mauna Loa summit.

104 Figure 4 shows a closer view of the seismicity in the summit region during
105 May-August (panels a-d). Seismic activity in May increases and is generally
106 diffuse, then changes into distinct arcuate bands throughout June-July, then
107 changes back into diffuse in August until it suddenly drops to background levels
108 on 3 August.

109 During this period the hypocenters migrated radially outward (map view;
110 epicentral distances with respect to reference location $(-155.285, 19.420)$) and
111 downward (cross-section view); Figure 5 shows hypocentral depths with time
112 beneath the Kīlauea summit region for 2018. This result shows that the peaks
113 in seismicity are concentrated between depths 0.5-2 km beneath the summit,
114 and throughout June-July they migrate about 200 m downward and 300 m
115 radially outward.

116 3.2. Seismic moment tensors

117 In our results the synthetic seismograms show good agreement with the
118 observations. The moment tensor uncertainty estimates for each event show
119 best fitting mechanisms that are localized toward the negative isotropic ($-ISO$)
120 region on the lunge; for details on the uncertainty analysis, see Alvizuri et al.
121 (2018). The supplement shows the best-fitting mechanisms for the 54 events
122 analyzed here, their waveform fits and uncertainty estimates.

123 The best-fitting moment tensors for the 54 M5s show consistent mechanisms
124 with their P-axes oriented vertically and magnitudes between M4.9–5.6 (Ta-
125 ble S2). The source durations for the first 5/54 events require source durations
126 that decrease from 20 to 5 seconds, while the remaining 49/54 events range be-
127 tween 1-2 seconds (Table S2). Figure 6 shows three periods of elevation models
128 for the summit region, together with the M5s, their shifting epicenters, and their
129 moment tensor beachballs.

130 The seismic moment tensor \mathbf{M} is a 3×3 mathematical matrix that represents
131 the seismic source and can be related with a single-process source model as
132 $M_{ij} = \mu(n_i s_j + n_j s_i) + \lambda \delta_{ij} \mathbf{S} \cdot \mathbf{N}$ (Aki & Richards, 1980), and Poisson's ratio
133 $\nu = \lambda/2(\lambda + \mu)$. In this model the seismic source \mathbf{M} represents (possibly oblique)
134 slip on a planar fault, and is characterized by the Lamé elastic parameters (λ, μ) ,
135 and an angle α between normal \mathbf{N} and slip \mathbf{S} vectors. For details, see Dufumier
136 & Rivera (1997); Tape & Tape (2013); and for applications in other settings in
137 the Earth's crust, see e.g. Alvizuri & Tape (2016); Alvizuri & Hetényi (2019).

138 We computed Poisson's ratio ν from the 54 events at Kīlauea and analyzed
139 their evolution. For the events up to June 25 their Poisson's ratios range between
140 $\nu = 0.1 - 0.3$; from June 26-on they converge to values near $\nu = 0.28$.

141 Figure 7 summarizes several observations and results with time: (a) moment
142 tensor focal mechanisms and accompanying seismicity; (b) median seismic mo-
143 ment and times of the M5s, tilt from station UWD (north component) near
144 the northwest caldera rim; (c) time difference between consecutive events and
145 Poisson's ratios estimated from the moment tensors.

146 4. Discussion

147 4.1. Moment tensors and collapse mechanisms

148 Seismic moment tensor studies for nuclear explosions at the Nevada Test
149 Site (NTS; USA) and Punggye-Ri (North Korea) reveal mechanisms with +ISO
150 parameters for the explosions; and secondary events following some explosions
151 show -ISO parameters and are presumed cavity collapses (e.g., Ford et al.,
152 2009; Chiang et al., 2014; Cesca et al., 2017; Alvizuri et al., 2018; Alvizuri &
153 Tape, 2018).

154 Our moment tensor results for the M5s at Kīlauea reveal consistent mecha-
155 nisms that converge toward -ISO, with vertical P-axes orientations, and with
156 source durations that decrease from ~ 20 to 5 seconds and converge to ~ 2 seconds
157 from May 30-onwards (Figures 6–8). Similar mechanisms were also observed
158 from the caldera collapse at Miyakejima (Shuler et al., 2013a) and Bárðarbunga
159 volcano (Gudmundsson et al., 2016). The moment tensors for Miyakejima show
160 source durations on the order of 50–60 seconds (these were not available for Bár-
161 darbunga), and both settings show mechanisms with vertical P axes (though the
162 analysis for Miyakejima was restricted to deviatoric moment tensors).

163 Seismic source studies at volcanoes often combine moment tensors with single
164 forces and complex geometries to study various processes such as fluid-rock
165 interaction (Kumagai et al., 2005; Chouet et al., 2010; Matoza et al., 2015), and
166 caldera collapse events (e.g., Kumagai, 2001; Duputel & Rivera, 2019). The
167 events we analyzed for Kīlauea may also arise from combinations of similar
168 processes, though the waveforms in our results show the moment tensor alone
169 adequately fits the observations.

170 Non-double-couple moment tensors may also arise as artifacts from imperfect
171 Earth models, anisotropy, curved faults, etc. (e.g., Kawasaki & Tanimoto, 1981;
172 Frohlich, 1994; Julian et al., 1998). These are known tradeoffs in full moment
173 tensor estimation, and can also be addressed with multiple force systems, finite
174 source studies (e.g., Fichtner & Tkalčić, 2010), more accurate structure models,
175 etc.

176 4.2. Collapse mechanisms and deformation

177 Field studies at NTS (e.g., Houser, 1969; Massé, 1981), at quarry sites (e.g.,
178 Scandone, 1990), and analogue sandbox experiments (Acocella, 2007; Ruch
179 et al., 2012) provide insight into the kinematic evolution of caldera collapses
180 from small (cm) to intermediate scales (100s m). They show block-like collapse
181 structures and fault systems that develop near the surface, with a range of radial
182 and concentric cracks and chimney collapse formations at depth.

183 In our analysis, the hypocenters in the summit region (including the M5s)
184 were concentrated between 0-3 km depth, and between May-August migrated
185 downward by about 200 m. During this period the summit crater caved down-
186 ward by up to 500 m while the crater rim expanded by about 1000 m. The epi-
187 centers in some areas form arcuate bands and radial streaks (depths 0.5~2.0 km),
188 and some large, shallower events (0~1.5 km depths) approximately follow the
189 expanding contours of the crater (Figure 6).

190 *4.3. Collapse and seismicity cycles*

191 During May-August, the seismicity beneath the summit region shows almost
192 daily cycles of escalating earthquake swarms that end with an M5 and are fol-
193 lowed by approximately 1 hr of relatively quiet periods ($N \leq 10$; similar patterns
194 were also observed by Shelly & Thelen (2019); Butler (2020)). This style in
195 cyclic seismicity continued until \sim Jun 28, where it changed into more sudden
196 onsets (the supplement shows additional views and shorter time windows).

197 The seismicity cycles also coincide with tiltmeter observations from station
198 UWD (Figure 7) to the west of the crater, which shows a long period trend of
199 tilt to the southeast, towards Halema‘uma‘u and intervening and periodic offsets
200 that coincide with the times of the M5s, and point away from Halema‘uma‘u.
201 A recent study (Segall et al., 2019) suggests that these trends follow a primarily
202 deflation process (revealed by subsidence at a GPS station at the Halema‘uma‘u
203 rim) and a secondary process of ash emissions as observed by the radially out-
204 ward transients (up to $89 \mu\text{rad}$ at UWD). Similar tiltmeter transients were also
205 observed on 2017 at Piton de la Fournaise (PdF), and may reflect a continuum
206 of deformation from the roof of the magma chamber to the surface (Michon
207 et al., 2007, 2009).

208 The episodic collapses at Kīlauea also appear coupled to pressure changes
209 within the magmatic system. A recent study estimated lava effusion rates at a
210 newly developed fissure in the LERZ using ground-based video and time-lapsed
211 images (Patrick et al., 2019), and they observe dual cycles in lava eruption
212 rates, one with periods of 5–10 minutes where effusion rates change from ~ 350 –
213 $1750 \text{m}^3 \text{s}^{-1}$; another as long-term surges in effusion rates and occurring no later
214 than 20 min after the collapse events, with effusion rates changing from ~ 300 –
215 $500 \text{m}^3 \text{s}^{-1}$ before collapse, up to $\sim 1400 \text{m}^3 \text{s}^{-1}$ after collapse. This suggests a
216 hydraulic connection where the summit reservoir provides pressurized magma to
217 the flank vents, in turn the flank vents regulate draining at the summit reservoir,
218 and where the summit collapse events induce pressure surges within the magma
219 conduits.

220 *4.4. Controls on times between collapses*

221 The events in the summit region group into two populations, depending
222 on their magnitudes at threshold $M_{\text{THR}}=4.4$. Similar M_{THR} values were also
223 observed in Miyakejima, Piton de la Fournaise and Fernandina (e.g. Michon
224 et al., 2011, and references there), and suggests similar collapse dynamics.

225 For the events in the summit region and $M < M_{\text{THR}}$, the time difference
226 between consecutive events T_{DIFF} approaches zero, and suggests the events are
227 not causally linked (e.g., Poisson distributed; Gardner & Knopoff, 1974). For
228 $M \geq M_{\text{THR}}$, T_{DIFF} varies between 10–60 hours until June 9, and from June 10–
229 onwards they converge on a trend that increases from about 20–40 hr.

230 T_{DIFF} together with a piston intrusion model (Kumagai, 2001), relates to
231 frictional difference F_{SD} , piston geometry and mass, and lava effusion rates.
232 These were variable for Kīlauea (e.g., Anderson et al., 2019; Patrick et al.,
233 2019). Nevertheless assuming all other variables constant, then $T_{\text{DIFF}} \propto F_{SD}$.

234 In other words, T_{DIFF} is in part controlled by rock mass, frictional difference,
235 magma draining rates, and possibly causally, where one event leads to the next.

236 *4.5. Collapse mechanisms and structure change*

237 The shallow magma reservoir beneath the Kīlauea summit region is esti-
238 mated to comprise a plexus of sills, dikes, magma filled cracks, and void space
239 (Fiske & Kinoshita, 1969; Dawson et al., 1999; Chouet et al., 2010; Johnson
240 et al., 2010). Towards the end of May the lava lake at Halema‘uma‘u crater was
241 no longer visible, which may indicate partial draining from the magma reservoir.

242 Core samples down to $\sim 1,200$ m beneath the summit region reveal mainly
243 basalt (Zablocki et al., 1974; Keller et al., 1979), and a seismic tomography
244 study for Kīlauea estimated Poisson’s ratios between $\nu = 0.25 - 0.32$ (Dawson
245 et al., 1999). Lab experiments where basalt samples are subjected to cyclic
246 loading show incremental Poisson’s ratios after each cycle, up to $\nu = 0.3$ (e.g.,
247 Schultz, 1993), and $\nu = 0.5$ for samples from Mt. Etna (Heap et al., 2009).

248 The Poisson’s ratios estimated from the M5s are initially variable ($\nu =$
249 0.3 to 0.1) and converge ($\nu \sim 0.28$) from June 26-onwards. These changes may
250 reflect similar loading cycles as observed in the lab, including possible mate-
251 rial changes, within a setting that becomes progressively consolidated and less
252 accommodating after each successive M5.

253 Brittle failure associated with structural collapse is consistent with the M5s
254 and broad seismicity features presented here. The pre-collapse Kīlauea summit
255 included, however, a complex magma and hydrothermal system; some of the
256 lower magnitude seismicity within the collapse sequence could be long-period
257 (LP) seismicity associated with magma-water interaction or water flashing to
258 steam as new contacts were made, old structural barriers breached, or pressures
259 released on fluid-filled voids (Chouet & Matoza, 2013, and references there).

260 Historically, the summit seismicity at Kīlauea includes shallow “LPC-A”
261 events which are observed in abundance accompanying rapid summit deflation,
262 after the onset of fountaining downrift at Pu‘u ‘Ō‘ō vent (Okubo & Nakata,
263 2003). In our analysis we found that 43/54 of the M5s associate with LPC-
264 A seismicity in the summit, which suggests the LPC-A events possibly share
265 similar collapse mechanisms as the M5s.

266 **5. Conclusion**

267 The 2018 caldera collapse at Kīlauea volcano was accompanied by 54 earth-
268 quakes ($M \sim 5$; M5s) and intervening seismicity which were concentrated beneath
269 the summit region down to ~ 3 km depths. We estimated seismic full moment
270 tensors for the M5s using waveform data from broadband seismic sensors, and
271 analyzed spatiotemporal changes in the intervening seismicity. The M5s and
272 intervening seismicity occurred in remarkable, almost daily succession, in con-
273 sistent styles, and suggests widely collapsing material.

274 The shallow M5s follow approximately the contours of the expanding crater
275 and appear related to the collapsing structures observed from aerial views. The
276 deeper M5s are concentrated between north and southeast of Halema‘ūma‘ū
277 pit crater. The moment tensors reveal consistent mechanisms with negative
278 isotropic parameters suggesting predominant material collapses, similar to chim-
279 ney collapses observed in analogue experiments and at nuclear explosion sites.

280 Poisson’s ratios estimated from the moment tensors are initially variable
281 ($\nu = 0.1 - 0.3$) and converge ($\nu \sim 0.28$) from June 26-onwards. These changes
282 may reflect loading cycles and material changes as observed in lab experiments,
283 and may reflect consolidating material after each successive M5.

284 The intervening seismicity forms into arcuate bands (map view) also east
285 and northeast of the crater; it migrated downward by ~ 200 m and radially
286 outward (map view) by ~ 300 m; and shares similar mechanisms as the M5
287 collapses which suggests a widely collapsing plexus. Further work estimating
288 source mechanisms for lower magnitude seismicity may confirm these results.

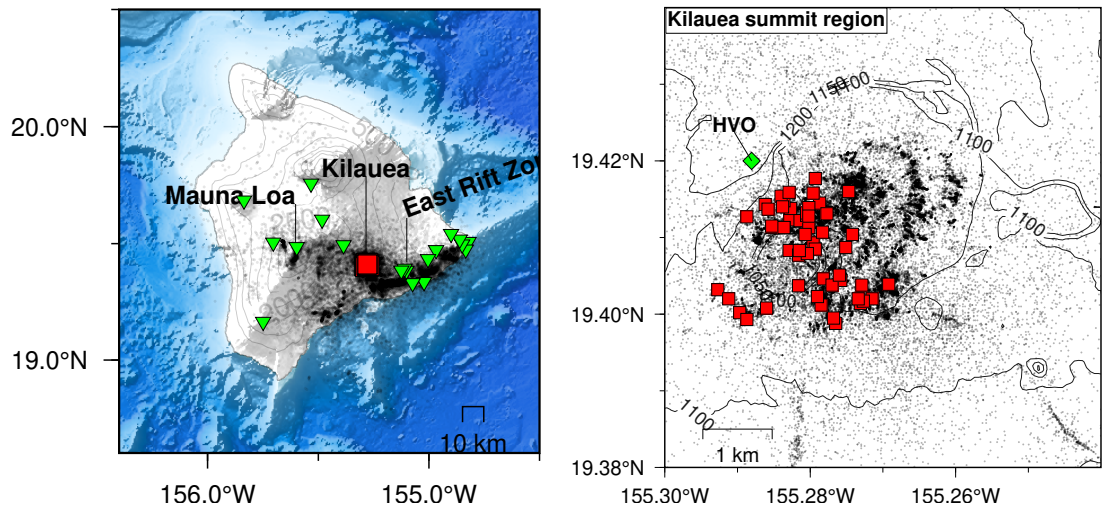


Figure 1: Seismicity in the Island of Hawai'i and in the Kīlauea summit region during 2018. Most of the seismicity was generated during the eruption at the Lower East Rift Zone and during the summit collapse at Kīlauea caldera (over 70,000 events; $M \geq 0$). We focus on the 54 major seismic events (red squares; $M \geq 5$) and intervening seismicity which occurred near Halema'uma'u pit crater in the Kīlauea summit region. We estimated seismic full moment tensors for the 54 events (M5s) using broadband waveform data from stations on the island (green triangles), and analyzed the spatial and temporal distribution of the intervening seismicity.

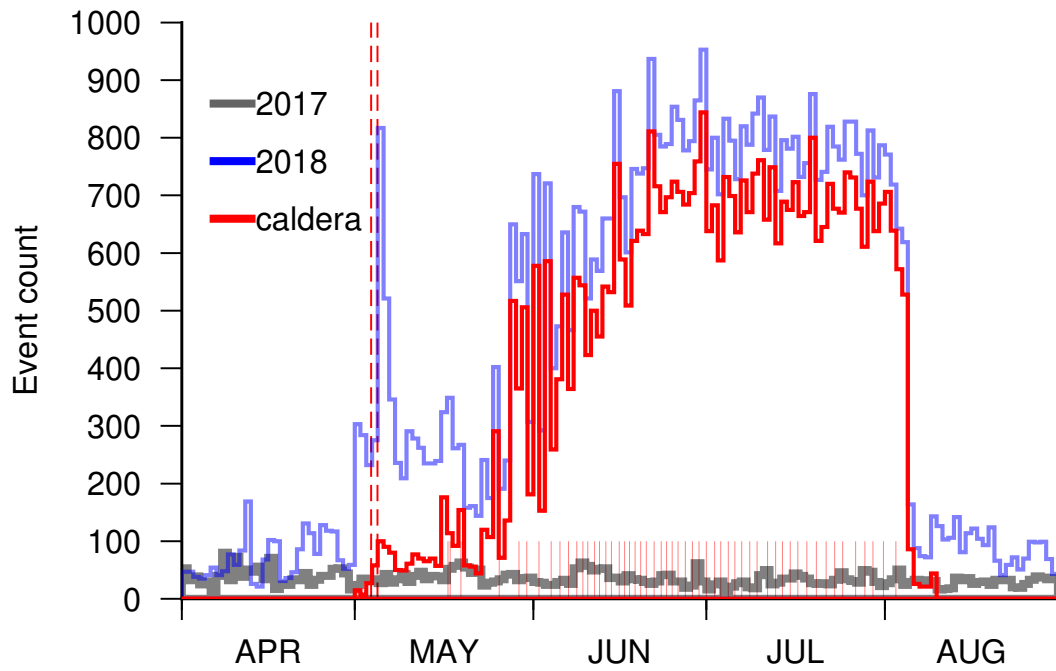


Figure 2: Seismicity levels in the Island of Hawai'i (blue) and in the Kīlauea summit region (red) during 2018 (the gray line shows reference seismicity levels during 2017). The daily seismicity at Kīlauea increased twice in May (red dashed lines) from background levels of ~ 30 events per day, to ~ 300 /day on 1 May 2018, and again to ~ 800 /day following the Mw 6.9 earthquake on 2018-05-04. The M5s (red short lines) and intervening seismicity occurred in succession between May-August.

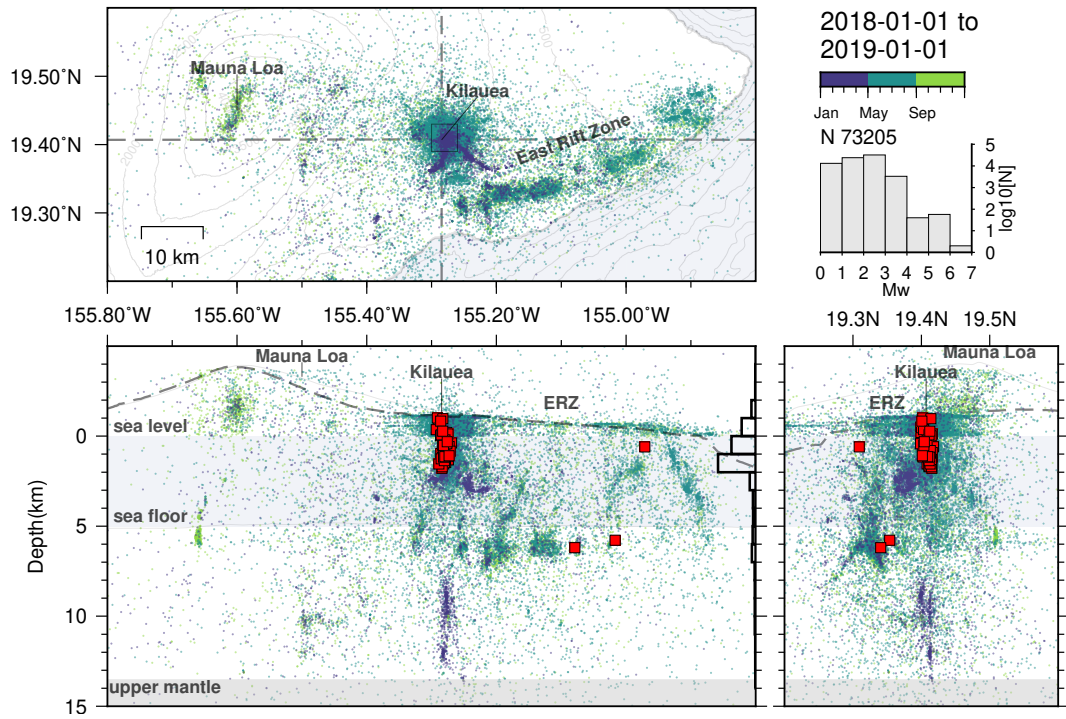


Figure 3: The M5s and seismicity in the southeast portion of the island during 2018. The seismicity (colored by time) until May was concentrated beneath the Kilauea summit region at depths 2-4 km and 7-13 km (bsl); it was followed by elevated seismicity in the summit region and the Lower East Rift Zone; then followed by the M5s and their intervening seismicity until August when seismic activity suddenly decreased to background levels. (Vertical exaggeration is 3X; the crosshairs are centered at Halema'uma'u pit crater.)

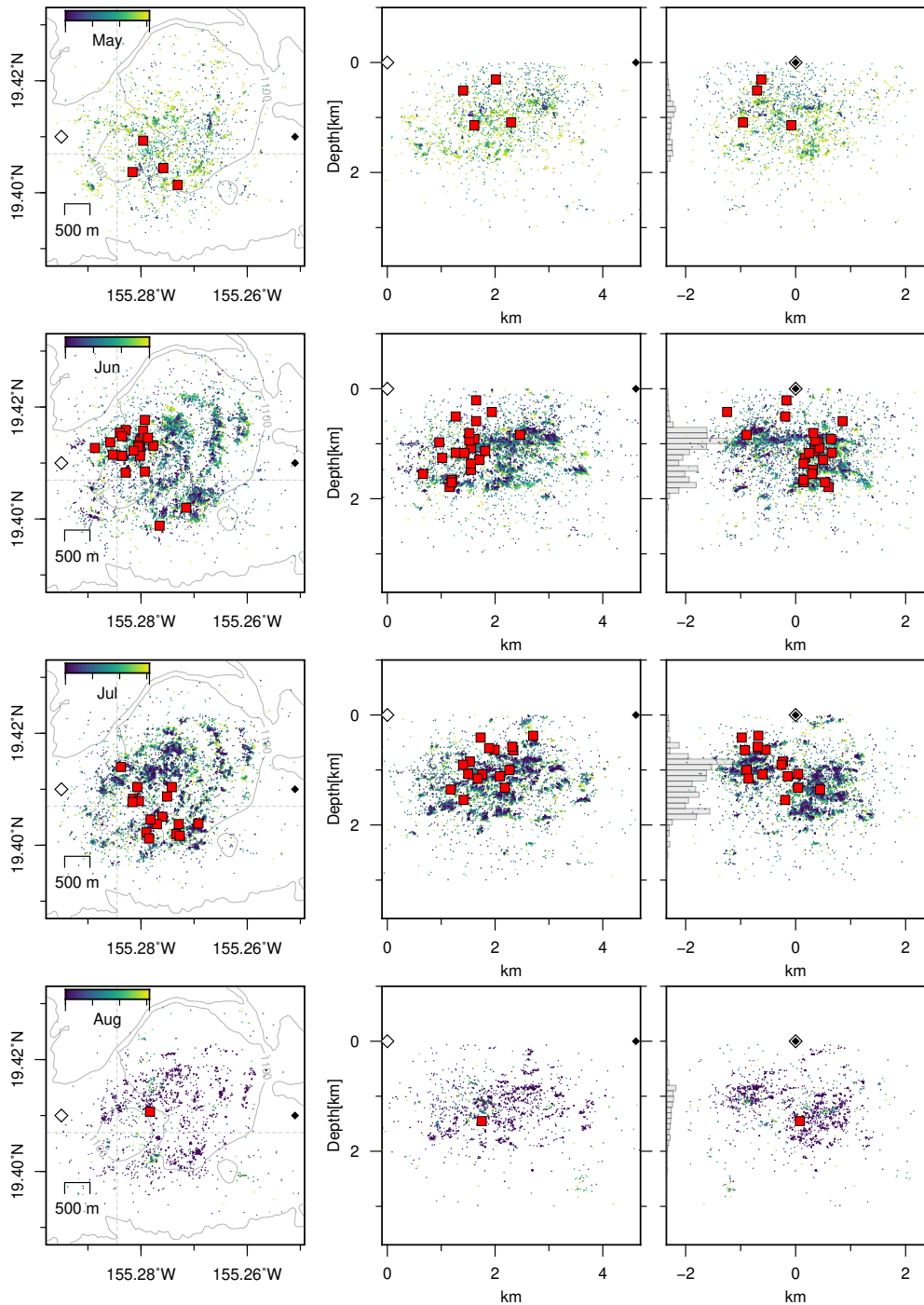


Figure 4: The M5s and intervening seismicity in the Kīlauea summit region from May-August, 2018. Each row shows one month of hypocenters (top row is for May, bottom row is for August). The left column shows map views; the center and right columns show cross-sections looking toward north and toward west. The M5s cluster to the north of Halema'uma'u crater (cross-hairs) in June, and to the east and southeast of the crater in July. The seismicity in map view forms into arcuate bands to the northeast of Halema'uma'u, which become prominent in June-July. During these months the seismicity migrated downward (cross-section view) and radially outward (map view).

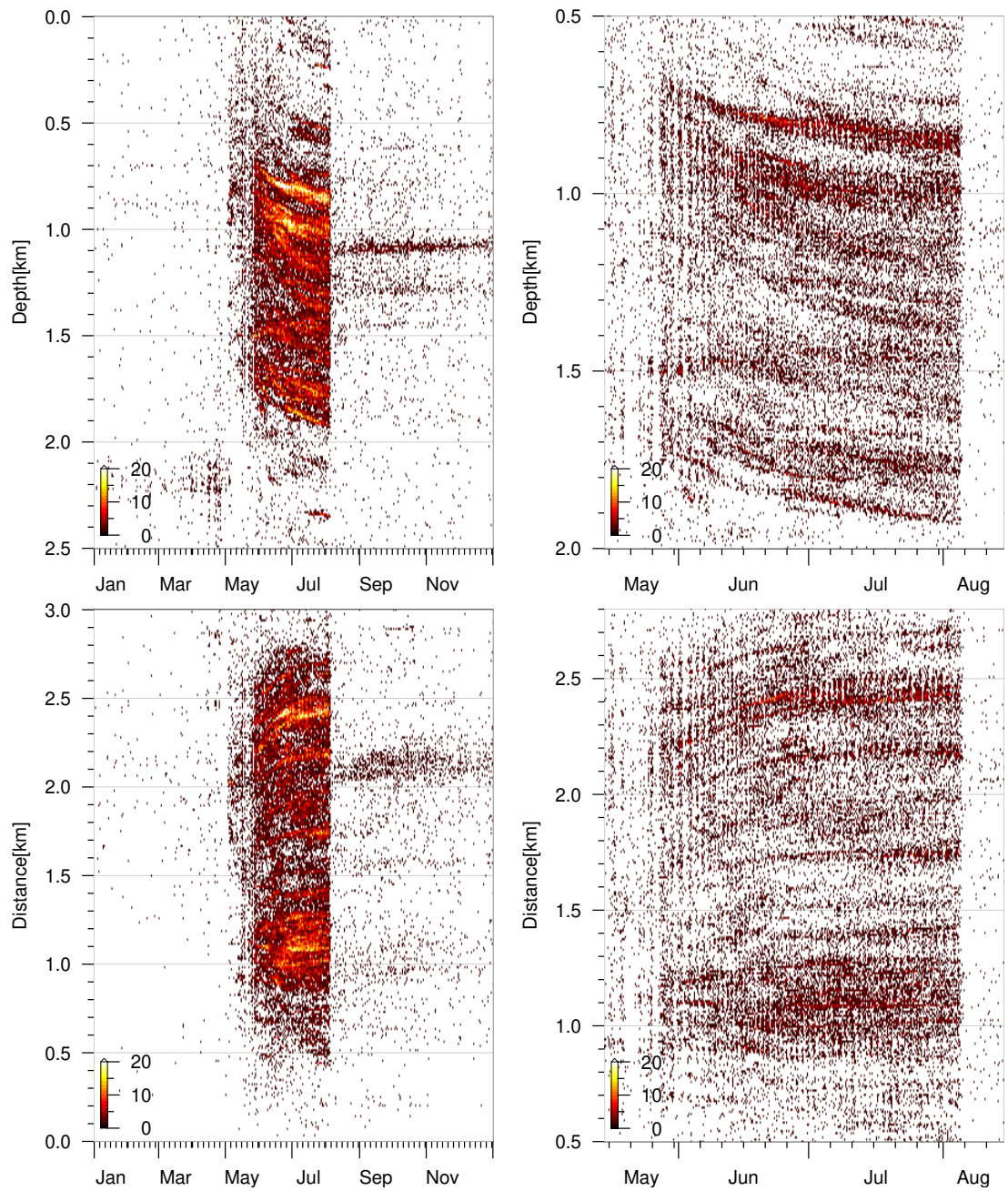


Figure 5: Between May-August the hypocenters in the Kīlauea summit region migrated downward by about 200 m (top panels) and radially outward by about 300 m (bottom panels). The heatmaps were computed using hypocenters within the same boundaries as in Figure 4, at 1-day bins and 10-meter depth intervals. The radial distances were computed from reference location $(-155.285, 19.420)$, north of Halema'uma'u crater.

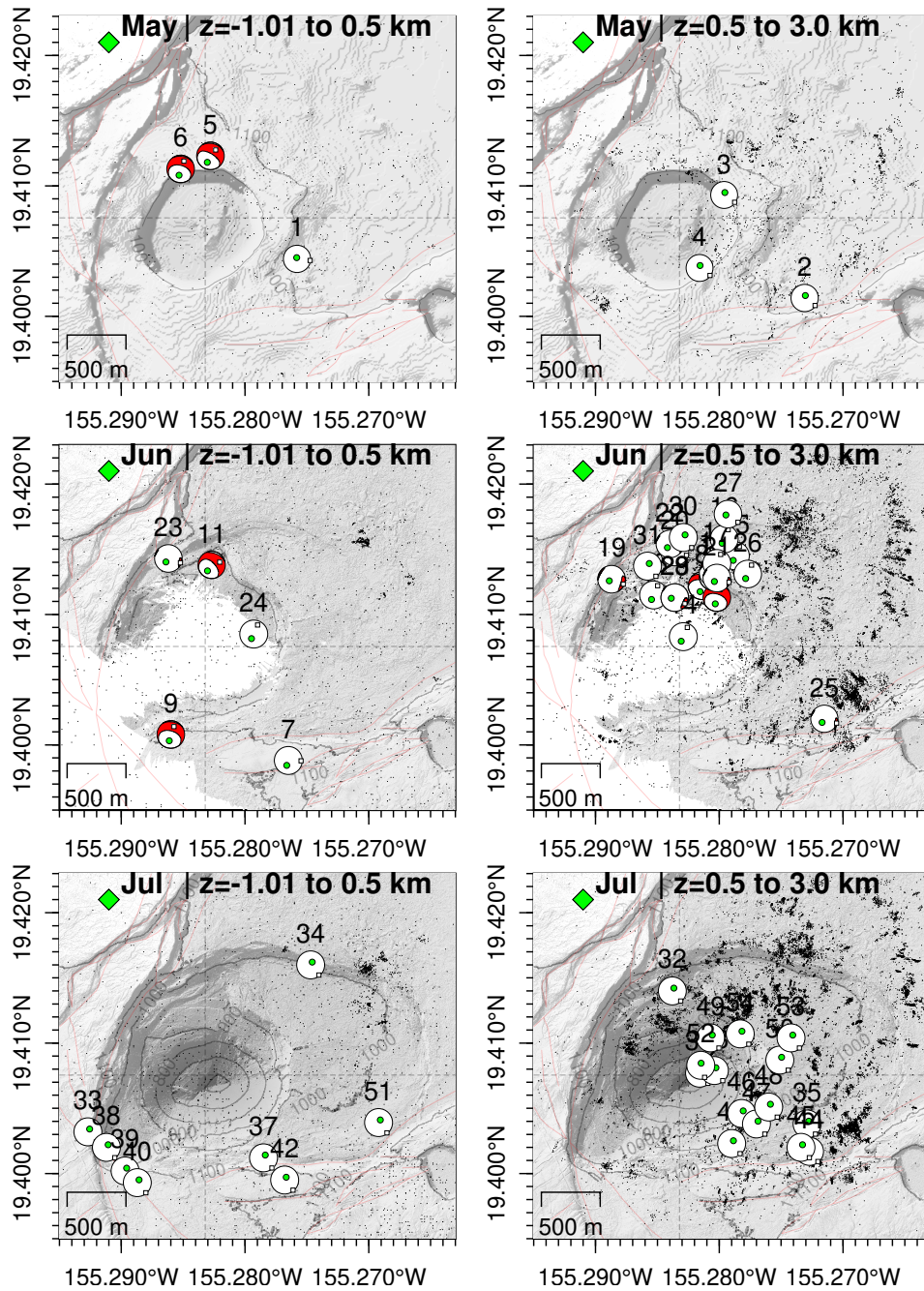


Figure 6: The M5s and their focal mechanisms (beachballs) between May-July, at two depth slices. The shallower M5s (depths -1 to 0.5 km bsl) approximately follow the expanding crater rim; while the deeper M5s cluster to the north of the previous crater (June), and to the east and southeast (July). Green circles denote the beachball P axes, which appear vertically oriented. The background elevation model for May is from ETOPO1, and for June-July from two LiDAR campaigns by the USGS. The green diamond shows tiltmeter station UWD.

Seismicity 2018-05-01 00:13:40 to 2018-08-09 22:56:20
 N 45228, tbin 1.0 hr

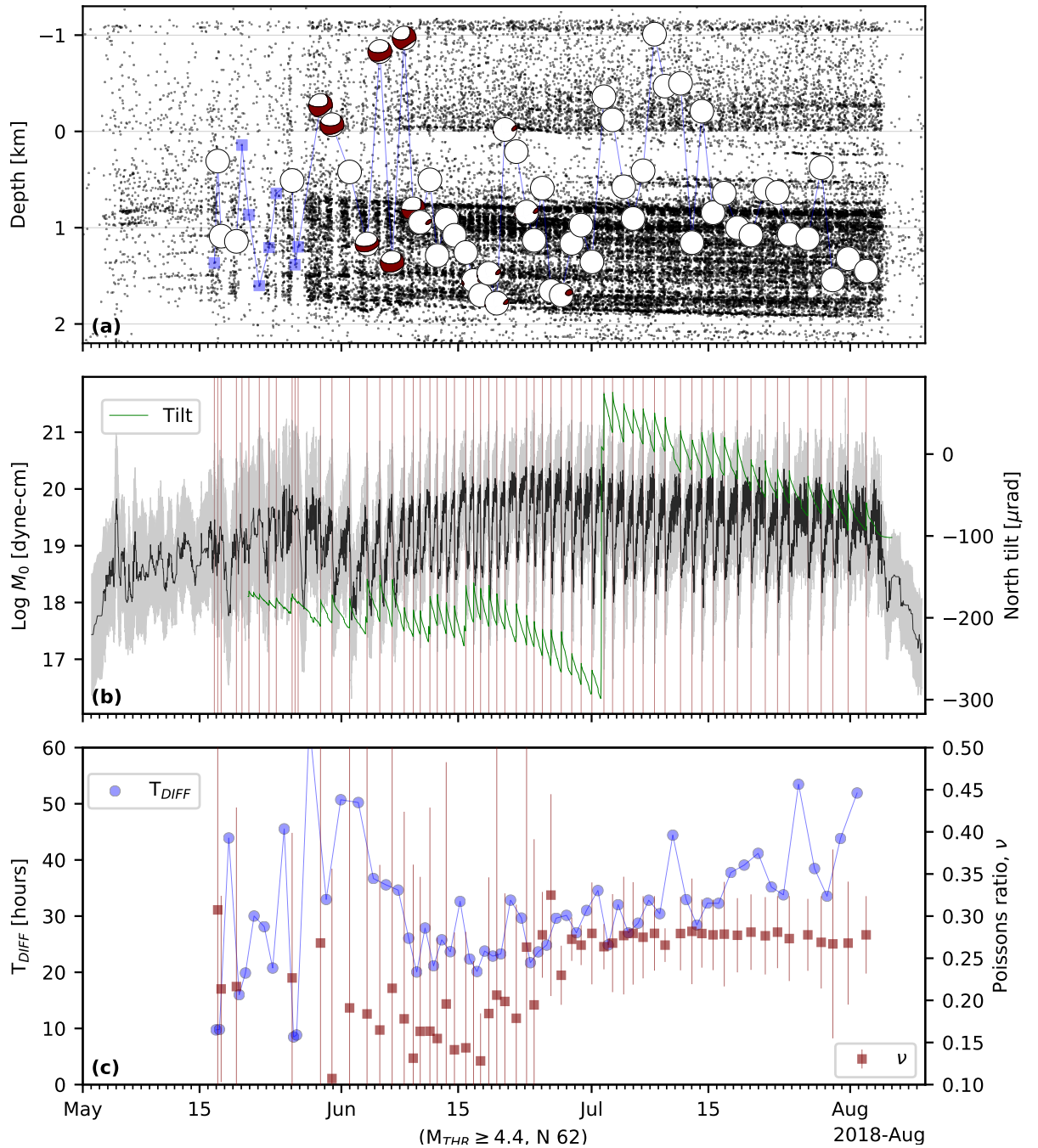


Figure 7: The M5s and their beachballs, together with intervening seismicity and tiltmeter data in the summit region. (a) beachballs in cross-section view (cf Figure 4) and hypocenters; (b) median seismic moment (black lines), mean absolute deviation (gray), times of the large events (red lines), and tiltmeter data (green) at station UWD (north component; the offset is due to recentering of the sensor); (c) time difference (T_{DIFF} ; blue circles) between consecutive events ($M_{THR} \geq 4.4$) and Poisson's ratios (red) estimated from the M5s.

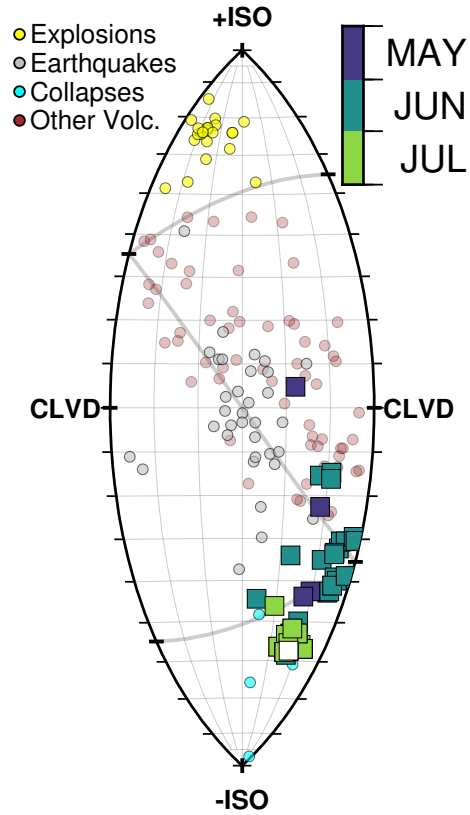


Figure 8: Lune representation of mechanisms from the M5s and other studies (Alvizuri & Tape, 2016; Alvizuri et al., 2018; Alvizuri & Tape, 2018). The lune provides a window into seismic moment tensors and organizes them into source type regions (e.g., Tape & Tape, 2019). Explosion mechanisms are on top (+ISO); collapses are on the bottom (−ISO); earthquakes are at the center (Figure S1 describes the lune in more detail). The M5s were remarkably consistent: they had similar magnitudes ($M \sim 5$); they occurred in orderly, almost daily succession; their mechanisms had similar orientations; and their source types converged towards −ISO and clustered tightly from July-onwards.

289 Acknowledgments

290 We thank Joël Ruch for illuminating discussions about faulting and col-
 291 lapse styles at Kīlauea and other calderas, and Carl Tape & Walter Tape for
 292 discussion about moment tensors. We thank the editor Dr. Hans Thybo and
 293 two anonymous reviewers whose comments helped to improve our manuscript.
 294 R.S.M. was supported by NSF grant EAR-1446543.

295 **References**

- 296 Acocella, V. (2007). Understanding caldera structure and development: An
297 overview of analogue models compared to natural calderas. *Earth-Sci. Rev.*,
298 *85*, 125–160. doi:10.1016/j.earscirev.2007.08.004.
- 299 Alvizuri, C., & Hetényi, G. (2019). Source mechanism of a lower crust earth-
300 quake beneath the Himalayas and its possible relation to metamorphism.
301 *Tectonophysics*, *769*, 128153. doi:10.1016/j.tecto.2019.06.023.
- 302 Alvizuri, C., Silwal, V., Krischer, L., & Tape, C. (2018). Estimation of full
303 moment tensors, including uncertainties, for nuclear explosions, volcanic
304 events, and earthquakes. *J. Geophys. Res. Solid Earth*, *123*, 5099–5119.
305 doi:10.1029/2017JB015325.
- 306 Alvizuri, C., & Tape, C. (2016). Full moment tensors for small events ($M_w < 3$)
307 at Uturuncu volcano, Bolivia. *Geophys. J. Int.*, *206*, 1761–1783. doi:10.1093/
308 gji/ggw247.
- 309 Alvizuri, C., & Tape, C. (2018). Full moment tensor analysis of nuclear ex-
310 plosions in North Korea. *Seismol. Res. Lett.*, *89*, 2139–2151. doi:10.1785/
311 0220180158.
- 312 Anderson, K. R., Johanson, I. A., Patrick, M. R., Gu, M., Poland, P. S. M. P.,
313 Montgomery-Brown, E. K., & Miklius, A. (2019). Magma reservoir failure
314 and the onset of caldera collapse at Kilauea Volcano in 2018. *Science*, *366*,
315 eaaz1822. doi:10.1126/science.aaz1822.
- 316 Butler, R. (2020). Volcanic earthquake foreshocks during the 2018 collapse of
317 Kīlauea Caldera. *Geophys. J. Int.*, *220*, 71–78. doi:10.1093/gji/ggz425.
- 318 Cesca, S., Heimann, S., Kriegerowski, M., Saul, J., & Dahm, T. (2017). Moment
319 Tensor Inversion for Nuclear Explosions: What Can We Learn from the 6 Jan-
320 uary and 9 September 2016 Nuclear Tests, North Korea? *Seismol. Res. Lett.*,
321 *88*, 300–310. doi:10.1785/0220160139.
- 322 Chiang, A., Dreger, D. S., Ford, S. R., & Walter, W. R. (2014). Source
323 characterization of underground explosions from combined regional moment
324 tensor and first-motion analysis. *Bull. Seismol. Soc. Am.*, *104*, 1587–1600.
325 doi:10.1785/0120130228.
- 326 Chouet, B. A., Dawson, P. B., James, M. R., & Lane, S. J. (2010). Seismic source
327 mechanism of degassing bursts at Kilauea Volcano, Hawaii: Results from
328 waveform inversion in the 10–50 s band. *Journal of Geophysical Research:*
329 *Solid Earth*, *115*, B09311. doi:10.1029/2009JB006661. 00056.
- 330 Chouet, B. A., & Matoza, R. S. (2013). A multi-decadal view of seismic meth-
331 ods for detecting precursors of magma movement and eruption. *J. Volcan.*
332 *Geothermal Res.*, *252*, 108–175. doi:10.1016/j.jvolgeores.2012.11.013.

- 333 Dawson, P. B., Chouet, B. A., Okubo, P. G., Villaseñor, A., & Benz, H. M.
 334 (1999). Three-dimensional velocity structure of the Kilauea Caldera, Hawaii.
 335 *Geophys. Res. Lett.*, *26*, 2805–2808. doi:10.1029/1999GL005379.
- 336 Dufumier, H., & Rivera, L. (1997). On the resolution of the isotropic component
 337 in moment tensor inversion. *Geophys. J. Int.*, *131*, 595–606.
- 338 Duputel, Z., & Rivera, L. (2019). The 2007 caldera collapse of Piton de
 339 la Fournaise volcano: Source process from very-long-period seismic signals.
 340 *Earth Planet. Sci. Lett.*, *527*, 115786. doi:10.1016/j.epsl.2019.115786.
- 341 Fichtner, A., & Tkalčić, H. (2010). Insights into the kinematics of a volcanic
 342 caldera drop: Probabilistic finite-source inversion of the 1996 Bárðarbunga,
 343 Iceland, earthquake. *Earth Planet. Sci. Lett.*, *297*, 607–615. doi:10.1016/j.
 344 epsl.2010.07.013.
- 345 Fiske, R. S., & Kinoshita, W. T. (1969). Inflation of Kilauea volcano prior to
 346 its 1967-1968 eruption. *Science*, *165*, 341–349.
- 347 Ford, S. R., Dreger, D. S., & Walter, W. R. (2009). Identifying isotropic events
 348 using a regional moment tensor inversion. *J. Geophys. Res.*, *114*. doi:10.
 349 1029/2008JB005743.
- 350 Frohlich, C. (1994). Earthquakes with non-double-couple mechanisms. *Science*,
 351 *264*, 804–809.
- 352 Gardner, J. K., & Knopoff, L. (1974). Is the sequence of earthquakes in Southern
 353 California, with aftershocks removed, Poissonian? *Bull. Seismol. Soc. Am.*,
 354 *64*, 1363–1367.
- 355 Geshi, N., Shimano, T., Chiba, T., & Nakada, S. (2002). Caldera collapse
 356 during the 2000 eruption of Miyakejima Volcano, Japan. *Bull. Volcanology*,
 357 *64*, 55–68. doi:10.1007/s00445-001-0184-z.
- 358 Gudmundsson, M. T., Jónsdóttir, K., Hooper, A., Holohan, E. P., Halldórsson,
 359 S. A., Ófeigsson, B. G., Cesca, S., Vogfjörð, K. S., Sigmundsson, F., Hög-
 360 nadóttir, T., Einarsson, P., Sigmarsson, O., Jarosch, A. H., Jónasson, K.,
 361 Magnússon, E., Hreinsdóttir, S., Bagnardi, M., Parks, M. M., Hjörleifsdóttir,
 362 V., Pálsson, F., Walter, T. R., Schöpfer, M. P. J., Heimann, S., Reynolds,
 363 H. I., Dumont, S., Bali, E., Gudfinnsson, G. H., Dahm, T., Roberts, M. J.,
 364 Hensch, M., Belart, J. M. C., Spaans, K., Jakobsson, S., Gudmundsson, G. B.,
 365 Fridriksdóttir, H. M., Drouin, V., Dürig, T., Aðalgeirsdóttir, G., Riishuus,
 366 M. S., Pedersen, G. B. M., van Boeckel, T., Oddsson, B., Pfeffer, M. A.,
 367 Barsotti, S., Bergsson, B., Donovan, A., Burton, M. R., & Aiuppa, A. (2016).
 368 Gradual caldera collapse at Bárðarbunga volcano, Iceland, regulated by lat-
 369 eral magma outflow. *Science*, *353*, aaf8988. doi:10.1126/science.aaf8988.
- 370 Heap, M. J., Vinciguerra, S., & Meredith, P. G. (2009). The evolution of elastic
 371 moduli with increasing crack damage during cyclic stressing of a basalt from

- 372 Mt. Etna volcano. *Tectonophysics*, *471*, 153–160. doi:10.1016/j.tecto.
373 2008.10.004.
- 374 Houser, F. (1969). Subsidence related to underground nuclear explosions,
375 Nevada Test Site. *Bull. Seismol. Soc. Am.*, *59*, 2231–2251.
- 376 Johnson, D. J., Eggers, A. A., Bagnardi, M., Battaglia, M., Poland, M. P.,
377 & Miklius, A. (2010). Shallow magma accumulation at Kīlauea Volcano,
378 Hawai‘i, revealed by microgravity surveys. *Geology*, *38*, 1139–1142. doi:10.
379 1130/G31323.1.
- 380 Julian, B. R., Miller, A. D., & Foulger, G. R. (1998). Non-double-couple earth-
381 quakes: 1. Theory. *Rev. Geophys.*, *36*, 525–549. doi:10.1029/98RG00716.
- 382 Kawasaki, I., & Tanimoto, T. (1981). Radiation patterns of body waves due to
383 the seismic dislocation occurring in an anisotropic source medium. *Bull. Seis-
384 mol. Soc. Am.*, *71*, 37–50.
- 385 Keller, G. V., Grose, L. T., Murray, J. C., & Skokan, C. K. (1979). Results of an
386 experimental drill hole at the summit of kilauea volcano, Hawaii. *J. Volcan.
387 Geothermal Res.*, *5*, 345 – 385. doi:10.1016/0377-0273(79)90024-6.
- 388 Krischer, L., Mengies, T., Barsch, R., Beyreuther, M., Lecocq, T., Caudron, C.,
389 & Wassermann, J. (2015). ObsPy: a bridge for seismology into the scientific
390 Python ecosystem. *Computational Science & Discovery*, *8*. doi:10.1088/
391 1749-4699/8/1/014003.
- 392 Kumagai, H. (2001). Very-Long-Period Seismic Signals and Caldera Forma-
393 tion at Miyake Island, Japan. *Science*, *293*, 687–690. doi:10.1126/science.
394 1062136.
- 395 Kumagai, H., Chouet, B., & Dawson, P. B. (2005). Source process of a long-
396 period event at Kilauea volcano, Hawaii. *Geophys. J. Int.*, *161*, 243–254.
397 doi:10.1111/j.1365-246X.2005.02502.x.
- 398 Laske, G., Masters, G., Ma, Z., & Pasyanos, M. E. (2013). Update on
399 CRUST1.0: A 1-degree global model of Earth’s crust. In *Geophys. Res. Ab-
400 stracts*. volume 15. Abstract EGU2013-2658.
- 401 Massé, R. P. (1981). Review of seismic source models for underground nuclear
402 explosions. *Bull. Seismol. Soc. Am.*, *71*, 1249–1268.
- 403 Matoza, R. S., Chouet, B. A., Dawson, P. B., Shearer, P. M., Haney, M. M.,
404 Waite, G. P., Moran, S. C., & Mikesell, T. D. (2015). Source mechanism of
405 small long-period events at Mount St. Helens in July 2005 using template
406 matching, phase-weighted stacking, and full-waveform inversion. *J. Geo-
407 phys. Res. Solid Earth*, *120*, 6351–6364. doi:10.1002/2015JB012279.
- 408 Matoza, R. S., Okubo, P. G., & Shearer, P. M. (2021). Comprehensive high-
409 precision relocation of seismicity on the Island of Hawai‘i 1986-2018. *Earth
410 and Space Sci.*, *8*. doi:10.1029/2020EA001253.

- 411 Matoza, R. S., Shearer, P. M., Lin, G., Wolfe, C. J., & Okubo, P. G. (2013).
412 Systematic relocation of seismicity on Hawaii Island from 1992 to 2009 using
413 waveform cross correlation and cluster analysis. *J. Geophys. Res.*, *118*, 2275–
414 2288. doi:10.1002/jgrb.50189.
- 415 Michon, L., Massin, F., Famin, V., Ferrazzini, V., & Roult, G. (2011). Basaltic
416 calderas: Collapse dynamics, edifice deformation, and variations of magma
417 withdrawal. *Journal of Geophysical Research*, *116*, B03209. doi:10.1029/
418 2010JB007636.
- 419 Michon, L., Staudacher, T., Ferrazzini, V., Bachèlery, P., & Marti, J. (2007).
420 April 2007 collapse of Piton de la Fournaise: A new example of caldera forma-
421 tion. *Geophysical Research Letters*, *34*, L21301. doi:10.1029/2007GL031248.
- 422 Michon, L., Villeneuve, N., Catry, T., & Merle, O. (2009). How summit calderas
423 collapse on basaltic volcanoes: New insights from the April 2007 caldera col-
424 lapse of Piton de la Fournaise volcano. *Journal of Volcanology and Geothermal*
425 *Research*, *184*, 138–151. doi:10.1016/j.jvolgeores.2008.11.003.
- 426 Minson, S. E., Dreger, D. S., Bürgmann, R., Kanamori, H., & Larson, K. M.
427 (2007). Seismically and geodetically determined nondouble-couple source
428 mechanisms from the 2000 Miyakejima volcanic earthquake swarm. *J. Geo-*
429 *phys. Res.*, *112*. doi:10.1029/2006JB004847.
- 430 Neal, C. A., Brantley, S. R., Antolik, L., Babb, J. L., Burgess, M., Calles, K.,
431 Cappos, M., Chang, J. C., Conway, S., Desmither, L., Dotray, P., Elias, T.,
432 Fukunaga, P., Fuke, S., Johanson, I. A., Kamibayashi, K., Kauahikaua, J.,
433 Lee, R. L., Pekalib, S., Miklius, A., Million, W., Moniz, C. J., Nadeau, P. A.,
434 Okubo, P. G., Parcheta, C., Patrick, M. R., Shiro, B., Swanson, D. A., Tollett,
435 W., Trusdell, F., Younger, E. F., Zoeller, M. H., Montgomery-Brown, E. K.,
436 Anderson, K. R., Pol, M. P., Ball, J. L., Bard, J., Coombs, M., Dietterich,
437 H. R., Kern, C., Thelen, W. A., Cervelli, P. F., Orr, T., Houghton, B. F.,
438 Gansecki, C., Hazlett, R., Lundgren, P., Diefenbach, A. K., Lerner, A. H.,
439 Waite, G., Kelly, P., Clor, L., Werner, C., Mulliken, K., Fisher, G., & Damby,
440 D. (2019). The 2018 rift eruption and summit collapse of Kīlauea Volcano.
441 *Science*, *363*, 367–374. doi:10.1126/science.aav7046.
- 442 Okubo, P., & Nakata, J. S. (2003). Tectonic pulses during Kīlauea’s current
443 long-term eruption. In C. Heliker, D. A. Swanson, & T. J. Takahashi (Eds.),
444 *The Pu’u ‘Ō’ō-Kūpaianaha Eruption of Kīlauea Volcano, Hawai’i; the First*
445 *20 Years* (pp. 173–186). Washington, D.C.: U.S. Geol. Survey. Professional
446 Paper 1676.
- 447 Patrick, M. R., Dietterich, H. R., Lyons, J. J., Diefenbach, A. K., Parcheta,
448 C., Anderson, K. R., Namiki, A., Sumita, I., Shiro, B., & Kauahikaua, J. P.
449 (2019). Cyclic lava effusion during the 2018 eruption of Kīlauea Volcano.
450 *Science*, *366*, eaay9070. doi:10.1126/science.aay9070.

- 451 Ruch, J., Acocella, V., Geshi, N., Nobile, A., & Corbi, F. (2012). Kinematic
452 analysis of vertical collapse on volcanoes using experimental models time se-
453 ries. *J. Geophys. Res. Solid Earth*, *117*, B07301. doi:10.1029/2012JB009229.
- 454 Scandone, R. (1990). Chaotic collapse of calderas. *Journal of Volcanology and*
455 *Geothermal Research*, *42*, 285–302. doi:10.1016/0377-0273(90)90005-Z.
- 456 Schultz, R. A. (1993). Brittle strength of basaltic rock masses with applica-
457 tions to Venus. *J. Geophys. Res. Planets*, *98*, 10883–10895. doi:10.1029/
458 93JE00691.
- 459 Segall, P., Anderson, K. R., Johanson, I., & Miklius, A. (2019). Mechanics
460 of Inflationary Deformation During Caldera Collapse: Evidence From the
461 2018 Kīlauea Eruption. *Geophys. Res. Lett.*, *46*, 11782–11789. doi:10.1029/
462 2019GL084689.
- 463 Shelly, D. R., & Thelen, W. A. (2019). Anatomy of a Caldera Collapse: Kīlauea
464 2018 Summit Seismicity Sequence in High Resolution. *Geophys. Res. Lett.*,
465 *46*, 14395–14403. doi:10.1029/2019GL085636.
- 466 Shuler, A., Ekström, G., & Nettles, M. (2013a). Physical mechanisms for
467 vertical-CLVD earthquakes at active volcanoes. *J. Geophys. Res.*, *118*, 1569–
468 1586. doi:10.1002/jgrb.50131.
- 469 Shuler, A., Nettles, M., & Ekström, G. (2013b). Global observation of vertical-
470 CLVD earthquakes at active volcanoes. *J. Geophys. Res.*, *118*, 1–27. doi:10.
471 1029/2012JB009721.
- 472 Silwal, V., & Tape, C. (2016). Seismic moment tensors and estimated uncer-
473 tainties in southern Alaska. *J. Geophys. Res. Solid Earth*, *121*, 2772–2797.
474 doi:10.1002/2015JB012588.
- 475 Simkin, T., & Howard, K. A. (1970). Caldera Collapse in the Galápagos Islands,
476 1968. *Science*, *169*, 429–437. doi:10.1126/science.169.3944.429.
- 477 Tape, W., & Tape, C. (2013). The classical model for moment tensors. *Geo-*
478 *phys. J. Int.*, *195*, 1701–1720. doi:10.1093/gji/ggt302.
- 479 Tape, W., & Tape, C. (2019). The eigenvalue lune as a window on moment
480 tensors. *Geophys. J. Int.*, *216*, 19–33. doi:10.1093/gji/ggy373.
- 481 Trugman, D. T., & Shearer, P. M. (2017). GrowClust: A Hierarchical Clustering
482 Algorithm for Relative Earthquake Relocation, with Application to the Span-
483 ish Springs and Sheldon, Nevada, Earthquake Sequences. *Seismol. Res. Lett.*,
484 *88*, 379–391. doi:10.1785/0220160188.
- 485 Zablocki, C. J., Tilling, R. I., Peterson, D. W., Christiansen, R. L., Keller,
486 G. V., & Murray, J. C. (1974). A deep research drill hole at the summit of
487 an active volcano, Kīlauea, Hawaii. *Geophys. Res. Lett.*, *1*, 323–326. doi:10.
488 1029/GL001i007p00323.

489 Zhu, L., & Rivera, L. A. (2002). A note on the dynamic and static displacements
490 from a point source in multilayered media. *Geophys. J. Int.*, *148*, 619–627.
491 doi:10.1046/j.1365-246X.2002.01610.x.